A Method for Estimating the Background Column Concentration of CO_2 Using the Lagrangian Approach

Zhipeng Pei, Ge Han, Xin Ma, Tianqi Shi, and Wei Gong, *Member, IEEE*

Abstract—With the rapid growth of greenhouse gas (GHG) monitoring satellites, more and more studies focused on the issue of inversion/optimization of carbon dioxide (CO_2) fluxes using satellite-derived XCO_2 observations in recent years. A common and critical challenge in this framework is the separation of background and anomalies from XCO_2 observations, which directly affect the performance of the CO_2 fluxes' inversion. We proposed a novel method to accurately extract background XCO_2 from satellite observations. A series of observing system simulation experiments (OSSEs) were performed to test the performance of the method. We found that the bias and uncertainty of the background concentration are below 0.01 and 0.05 ppm in the given cases, respectively. Based on this method, we selected five overpasses from 2014 to 2016 to demonstrate a regional-scale flux inversion near Riyadh. The comparison with the two previous methods shows that the posterior simulated XCO_2 by the method proposed in this article can match better with the observed XCO_2 from Orbiting Carbon Observatory-2 (OCO-2).

Index Terms—Background concentration, carbon, flux inversion.

I. INTRODUCTION

CARBON dioxide (CO_2) is an important anthropogenic greenhouse gas (GHG), accounting for about 65% of the total radiative forcing of long-lived GHGs [1]. A few years after signing of the Paris Climate Agreement, several countries, including the Europe Union, China, and Japan, have announced ambitious carbon neutral plans. President Biden signed an executive order to rejoin the Paris Climate Agreement on his first day as the President of U.S., exhibiting the determination of his administration to solve the climate issue. Accurate carbon accounting is the basis for developing scientific and effective mitigation measures. It is thus urgently needed to upgrade current means to accurately and timely estimate CO_2 emissions/fluxes with a finer spatial and time scale.

Previous studies have used "bottom-up" and "top-down" methods to quantify anthropogenic CO_2 emissions [2]–[5]. The Intergovernmental Panel on Climate Change (IPCC) recommends the bottom-up approach to estimate fossil fuel (FF) CO_2 emissions at different scales [6], relying on activity data and emission factors derived from a combination of *in situ* observations and simulation studies. Such an approach provides a common criterion for different countries and regions to compile their own CO_2 emission inventories, greatly contributing to our understanding of CO_2 emissions. However, evident uncertainties in emission estimates were reported, varying from 5% to nearly 50% [7]. For example, Liu *et al.* [8] noted that the emission factor for Chinese coal is on average 40% lower than the default value recommended by the IPCC, and that the use of different sources of official activity data and emission factors can result in estimated emissions varying by up to 40% in a given year. Uncertainty in the activity data and emission factors has been shown to range from 10% to 40% at national scales and over 150% at urban scales [5], [9], [10]. Besides, the timely and rapid updating of emission inventories is a formidable challenge facing the bottom-up approach.

To supplement the bottom-up approach, the top-down approach uses atmospheric observations and inversion techniques to estimate CO_2 fluxes at regional to global scales. Ground-based or airborne observations can help constrain the inversion of CO_2 emissions [2], [11]–[13]. With advances in satellite remote sensing technology, it has become possible to obtain dense, XCO_2 observations with a high precision on a global scale, which has greatly facilitated the widespread use of the top-down methods [14], [15]. The launch of Orbiting Carbon Observatory-2 (OCO-2) provides scientists with an opportunity to measure XCO_2 from the space, and thus determines the location of carbon sources and sinks using atmospheric transport models. OCO-2's sun-synchronous orbit allows it to acquire observations at about 1:30 P.M. local time, yielding a high signal-to-noise ratio (SNR) and good quality. However, such an orbit also results in a long revisit period and low data volumes. Most of the related studies focus on forward modeling to prove that OCO-2 is capable of detecting the signal due to urban anthropogenic carbon emissions [16]–[18]. Quantitative estimates of anthropogenic carbon emissions using satellite XCO_2 products have become the focus of subsequent studies [19], [20]. The key step in the top-down approach is to build a bridge between the flux and

the concentration using some atmospheric transport models. The decomposition of CO_2 concentration into enhancement and background concentration is critical for flux inversion. Previous studies demonstrate that imperfect determinations of the CO_2 background concentration will lead to large errors in the CO_2 flux inversion [5], [17], [21].

Researchers used distinct methods to derive XCO_2 background. In general, these methods can be grouped into two main categories. The first one is the statistical method [22], [23]. Its major feature is to neglect the atmospheric transport process and deduce XCO_2 background based only on XCO_2 observations themselves. For example, a few studies defined the background concentration as mean XCO_2 value over "clean area" (e.g., desert north to Los Angeles) unaffected by anthropogenic activities [24], [25]. Ye *et al.* [16] used a two-step linear regression to obtain the "background line." The other one is the trajectory-endpoint method [5], [26], [27], which is often used to explain large CO_2 anomalies, such as the CO_2 enhancement caused by wildfires [17], [28]. Its core idea is to use some atmospheric transport models to identify regions that are not affected by anthropogenic CO_2 fluxes. On that basis, one can use XCO_2 over those regions as the background. For example, Hu *et al.* [5] released air parcels and tracked where the parcels were located seven days ago and determined the background concentration based on the Carbon Tracker 3-D CO_2 product. The determination of XCO_2 background exerts evident impacts on subsequent fluxes inversions. Wu *et al.* [17] figured out that a mean difference of -0.55 ppm in background concentration could lead to a 39% higher mean observed urban signal and a larger scaling factor. Nassar *et al.* [20] and Fischer *et al.* [29] also witnessed the effect of biases in XCO_2 background on their flux optimization recently.

To address this issue, we introduce a new method to determine the CO_2 background concentration. Based on the hypothesis that the difference between the simulated and observed CO_2 concentrations satisfies a normal distribution ($\mu = 0$), we use a Bayesian inversion method, considering both the trustworthiness of the prior fluxes and the observations, and linking the two through an atmospheric transport model to accomplish an accurate estimation of the CO_2 background concentration. To quantitatively evaluate the performance and sensitivity of the proposed new method, we constructed an observing system simulation experiments (OSSEs) to perform simulation experiments by the Monte Carlo methods. On that basis, we further applied the proposed method to CO_2 flux inversion experiments using actual OCO-2 XCO_2 products to test its validity in real cases. The remaining parts of this work are organized as follows. In Section II, we introduce the background XCO_2 estimation method proposed in this work in detail, as well as the models and data involved in the subsequent experiments. In Section III, the sensitivity analysis on the proposed method was demonstrated using OSSEs to test the robustness. We compared the differences between the results obtained by our method and the previous ones in Riyadh using real OCO-2 XCO_2 products. Sections IV and V discuss the sensitivity experiments and summarize the whole study, respectively.

II. MATERIALS AND METHODS

A. STILT Configuration

The Stochastic Time Inverted Lagrangian Transport (STILT) [30] is an atmospheric transport model, which relates the CO_2 surface flux upstream of the observation point to the XCO_2 enhancements using footprint weights. The specific principle is to simulate the backward trajectory of the air parcels driven by the wind via releasing a large number of air particles backward and to quantify the value of the footprint weight by calculating the number of all particles and the residence time of each particle within the surface layer height (usually half of the planetary boundary layer (PBL) height) in a region upstream [30], [31].

The STILT model is driven by the meteorological field with a high precision output from the Weather Research and Forecasting (WRF) model. The initial meteorological field used by the WRF model is from Final Operational Global Analysis (FNL) data from the National Centers for Environmental Prediction (NCEP) (rda.ucar.edu/datasets/ds083.2). Three nested domains with respective horizontal resolutions of 27, 9, and 3 km, and 51 vertical levels are used. The physics configurations are the same as a study over Middle East of Yesubabu *et al.* [32]: Dudhia short-wave radiation scheme, rapid radiation transfer model long-wave radiation scheme, and Yonsei University non-local scheme for the PBL.

A proper setting of the receptor (location of released air particles) height and backward time in the STILT model is critical for any actual inversion experiments. Besides, the maximum release height (maximum release height (MAXAGL), in meters above ground level) setup faces a similar problem. We conducted some pre-tests in the study area to find a reasonable setting of the backward time and the MAXAGL. We noted that when the backward time is longer than 70 h and the MAXAGL is larger than 4 km, the footprint values hardly increased any more. Therefore, we used a MAXAGL of 6 km during the winter months and a backward time of 72 h in this study. Column receptors are located every 100 m from the ground to 3 km and every 500 m from 3 to 6 km, following Wu *et al.*'s [17] work. At each layer below the MAXAGL, 500 air parcels are released.

B. Novel Background XCO_2 Optimizer

1) Approach Summary: In this study, the background XCO_2 is defined as the regionally uniform XCO_2 unaffected by local anthropogenic emissions and natural fluxes. The determination of the background XCO_2 plays an important role in the inversion of carbon emissions. For example, an underestimated background XCO_2 can lead to an overestimation of anthropogenic carbon emissions [17].

The proposed background XCO_2 extraction method was derived from a forward model and an inversion framework. We then designed a core optimizer via formula derivation and some specific assumptions. The forward model is used to establish the relationship between the *a priori* CO_2 flux and XCO_2. Its key parameter is the footprint of the XCO_2 observations calculated using an atmospheric dispersion model, namely, the Weather Research and Forecasting [33]-Stochastic Time Inverted Lagrangian Transport [30] (WRF-STILT) model

used in this work. The inversion framework is responsible for estimating the *a posteriori* CO$_2$ flux using actual XCO$_2$ observations and the background XCO$_2$. The core optimizer compares the difference between the posterior simulated XCO$_2$ outputs from the forward model and the XCO$_2$ observations of OCO-2 and implements the optimization process by adjusting the background XCO$_2$ so that the differences between the simulated XCO$_2$ and measured XCO$_2$ satisfy a normal distribution [$\mathcal{N}(0, \sigma^2)$]. The inversion framework can optimize the flux and thus indirectly evaluate the accuracy of the background XCO$_2$.

2) Forward Model: In this study, the simulated XCO$_2$ (XCO$_2^m$) is composed of the background concentration (XCO$_2^{bg}$), the contribution of net ecosystem exchange (NEE) (XCO$_2^{nee}$), and the contribution of FFs (XCO$_2^{ff}$), as shown in the following equation:

$$XCO_2^m = XCO_2^{bg} + XCO_2^{nee} + XCO_2^{ff}. \quad (1)$$

OCO-2 provides a CO$_2$ profile of typically 20 layers, depending on the pressure of each layer, from 0 hPa to surface pressure [34], [35]. The pressure weighing function and the averaging kernel (AK) represent the relationship between the true profile and the *a priori* profile [17], [34], [36], [37]. We use the same pressure weighting function as for OCO-2. The simulated CO$_2$ profile serves as the true profile. Thus, the simulated, OCO-2-like XCO$_2$ (XCO$_2^m$) can be obtained by (3), following Wu *et al.* [17]

$$XCO_2^m = XCO_2^a - \sum_{i=1}^{n} x_i^a h_i a_i + \sum_{i=1}^{n} x_i^m h_i a_i \quad (2)$$

where XCO$_2^a$ is the OCO-2 *a priori* column concentration, and x_i^a is the *a priori* concentration of the *i*th layer. h_i and a_i are the pressure weighting function and the average kernel of the *i*th layer, respectively. x^m is the simulated profile from the WRF-STILT model. Since the pressure levels of particle release heights we set in the model are not consistent with those of OCO-2, the interpolation of h and a is required, as detailed in Wu *et al.*'s [17] study.

The footprint derived from STILT describes the sensitivity of observations to fluxes contributing to the CO$_2$ concentration at each selected receptor location and time. In addition, the weighted column footprint (Xfootprint) that describes the sensitivity of enhancements of XCO$_2$ due to upwind surface fluxes is introduced by Wu *et al.* [17], as shown in the following equations:

$$\text{Xfootprint} = \sum_{i=1}^{n} \text{footprint}_i \times h_i \times a_i \quad (3)$$

where footprint$_i$ is the footprint of the receptor in the *k*th layer. Fig. 1 shows the footprint at different altitudes and the Xfootprint. Finally, we can obtain the simulated XCO$_2$, as indicated by (2) and (3).

3) Inversion Framework: The inversion framework of surface CO$_2$ fluxes consists of a footprint generating module and a Bayesian inversion module. The Bayesian inference is widely used to estimate CO$_2$ fluxes using measurements of atmospheric CO$_2$ concentrations. First, the relationship
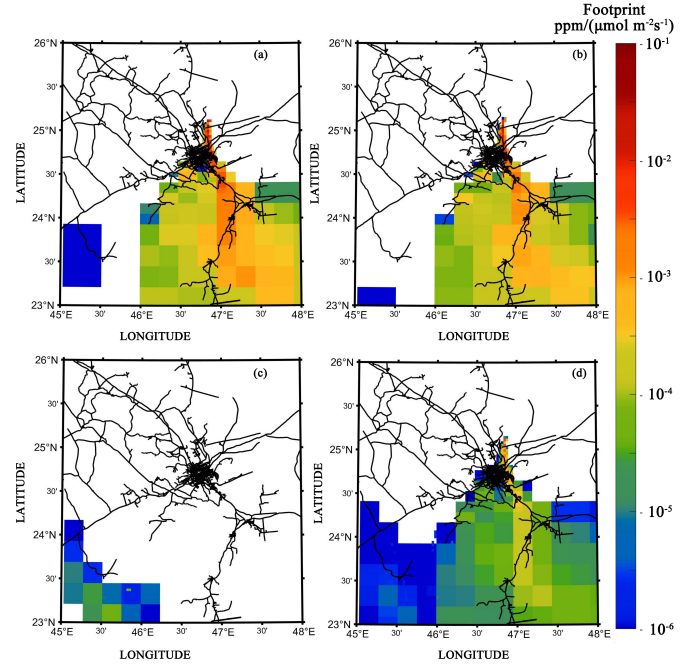

Fig. 1. Footprint at different fixed altitudes and the Xfootprint at 10:00 UTC on Riyadh where the receptor is placed at 25.2°N, 46.8°E. The fixed receptors were placed every 100 m within 3 km and every 500 m from 3 to 6 km. (a)–(c) Footprints of the receptors located at 500, 1000, and 1200 m altitude, respectively. (d) Xfootprint weighted by the pressure weighting functions and AK. The black lines indicate roads in Saudi Arabia to represent areas of human activity.

between the high-resolution CO$_2$ inventory (*x*, an $m \times 1$ vector) and observations of atmospheric CO$_2$ concentrations (*y*, an $n \times 1$ vector) can be described as follows:

$$y = Kx + \epsilon \quad (4)$$

where K is an $n \times m$ Jacobian matrix, a reshaped footprint. n and m represent the number of observations and the number of grids of the surface fluxes, respectively. The footprint in this work means the sensitivity of XCO$_2$ measured at a given location to upstream surface CO$_2$ fluxes. ϵ is an $n \times 1$ vector, representing normally distributed noise with mean ϵ_b and a diagonal covariance matrix $R(\epsilon \sim \mathcal{N}(\epsilon_b, R))$. We assume the mean bias is zero, and the mismatch errors are uncorrelated. The cost function [38]–[40] is defined as follows:

$$\chi^2 = (x - x_a)^T S_a^{-1}(x - x_a)$$
$$+ \left(y - XCO_{2,bg} - Kx\right)^T S_\varepsilon^{-1}\left(y - XCO_{2,bg} - Kx\right) \quad (5)$$

where $S_a(m \times m)$ and $S_\varepsilon(n \times n)$ represent the *a priori* flux error covariance and the observation error covariance matrix, respectively. Following Villalobos *et al.* [37], Lauvaux *et al.* [41], Meirink *et al.* [42], and Turner *et al.* [39], the *a priori* error covariance matrix can be expressed in terms of the correlation matrix and the diagonal variances matrix, $S_a = V^{1/2} M V^{1/2}$, where V is the diagonal matrix of variances and M is the correlation matrix. The correlation decays exponentially with the distance. The correlation length was assumed to be 5 km following Turner *et al.* [39]. We assumed no temporal error correlation between two overpasses we used, which differs

from Chevallier *et al.* [53] who used a temporal correlation length of four weeks. S_ε represents any uncertainties related to the XCO_2 observations and forward model. The uncertainty of OCO-2 observations can be set according to the "XCO_2 uncertainty" variable in the OCO Lite product [34]. The estimation of transport error is detailed in Section II-D. x_a is the $m \times 1$ vector of a prior fluxes. We need to find the optimal flux to minimize the cost function. As shown in the following equation, we can get an optimal CO_2 flux assuming that the prior and likelihood distribution are Gaussian [38]–[40]:

$$x_p = x_a + S_p K^T S_\varepsilon^{-1}(y - XCO_{2,b\ g} - Kx_a). \quad (6)$$

Some previous studies used the *a posteriori* error covariance $(S_p = (K^T S_\varepsilon^{-1} K + S_a^{-1})^{-1})$ to evaluate the accuracy improvement [11], [43]. The AK matrix $(A = S_p K^T S_\varepsilon^{-1} K)$ and the degrees of freedom (DOFs) for signal [DOFs = tr(A)] are used to evaluate the information content [37].

4) Core Optimizer: When we consider the background concentration as an unknown constant, we can get an optimized *a posteriori* flux. The differences between *a posteriori* simulated XCO_2 and measured XCO_2 should satisfy a normal distribution with a mean of 0 [$\epsilon \sim \mathcal{N}(0, \sigma)$]. $XCO_{2,bg}$ can be derived from the following equation:

$$XCO_{2,bg} = -\frac{\text{sum}(y - Kx_a - KS_p K^T S_\varepsilon^{-1}(y - Kx_a))}{\text{sum}(\text{sum}(KS_p K^T S_\varepsilon^{-1}, 2) - 1)} \quad (7)$$

where sum(X) is the sum of the 1-D matrix X and sum(Y, 2) is the sum of each row of the 2-D matrix Y.

Note that the inversion framework and the background optimizer are two independent processes. We first use the optimizer to obtain an estimate of the background XCO_2, and then use this result to perform the inversion process.

C. Experimental Data

We focus on a small spatial domain (from 45°E to 48°E, from 23°N to 26°N) to extract background XCO_2 and then to perform a Bayesian inversion. The spatial distribution of the experimental data examples (including XCO_2 observations and fluxes) used in this work is shown in Fig. 2. Partial information of these datasets is shown in Table I.

1) Study Area: Riyadh (latitude 25°N, longitude 47°E) is the capital and the largest city of the West Asian country of Saudi Arabia and capital of Riyadh province, with a population of over 6 million [44]. Riyadh with tropical desert climate is preferred in this work because of low cloud disturbances and a low vegetation cover [16], [17], [36]. These factors help OCO-2 to obtain better quality data. Secon, Riyadh has the highest CO_2 emissions in the Middle East [45].

2) OCO-2 XCO_2 Observations: The OCO-2 was launched on July 2, 2014, to quantify CO_2 in the atmosphere from space with sufficient accuracy [46], [47]. The OCO-2 obtains surface-reflected solar radiance at 0.76 μm oxygen A-band, and 1.61 and 2.06 μm CO_2 band to retrieve the column-averaged dry air mole fraction of CO_2 (XCO_2) [35]. As a member of the A-Train constellation, OCO-2 flies on a Sun-synchronous orbit and crosses the equator at approximately 13:30 local time every day [48].

In this study, we used $OCO_2\_L2\_Lite\_FP$ 9r data [49] from December 2014 to February 2016 provided by NASA's Jet Propulsion Laboratory. We selected available data near the downwind direction of Riyadh. Soundings with a poor quality ($XCO_2\_quality\_flag = 1$) were filtered out. The retrieval algorithm details the pressure weighting function, average kernel, and optimal estimation approach [34].

3) FF CO_2 Emissions: We used products from the Emissions Database for Global Atmospheric Research (EDGAR) to construct our *a priori* FF fluxes. Table I demonstrates the key features of the global high-resolution gridded anthropogenic emissions data product used in this work. EDGARv5.0 provides the emissions of the three main GHGs (CO_2, CH_4, and N_2O) for each sector and country [50]. For energy-related sectors, the activity data are mainly based on the International Energy Agency (IEA) energy balance statistics, while the activity data of the agricultural sector mainly come from the Food and Agriculture Organization (FAO) of the United Nations. Since the resolution of the WRF-generated meteorological field is 3 km $\times$ 3 km, we resampled the *a priori* flux to that resolution. Besides, the gridded emission data provided by EDGARv5.0 are annual. We need to obtain monthly fluxes to match satellite-derived XCO_2 observations. In this work, we used monthly scaling factors, as shown in Fig. 3, provided by the Carbon Tracker to obtain the monthly FF fluxes using EDGARv5.0.

4) Biogenic Fluxes: The NEE data are provided by the Carbon Tracker [2] with a spatial resolution of 1° $\times$ 1° and a temporal resolution of 3 h. The *a priori* NEE is simulated using the Carnegie-Ames-Stanford Approach (CASA) [51] model and normalized difference vegetation index (NDVI) [52] values from remotely sensed observations. Based on the global CO_2 concentration observations and the atmospheric transport model (TM3), a Bayesian inversion is performed to optimize the *a priori* NEE so that the simulated concentration values best match the observed values. Positive values represent carbon sources and negative values represent carbon sinks.

D. Observing System Simulation Experiments

Referring to Chevallier *et al.* [53], our OSSEs' flowchart is shown in Fig. 4. We assume that the true background XCO_2 is 397 ppm. The prescribed EDGAR FF fluxes are assumed as the true fluxes to be retrieved. The meteorological field we obtained near Riyadh on December 29, 2014, is assumed to be true at this stage, which means that the footprint we obtained is unbiased. In Section IV, we further analyze the effect of errors in the atmospheric transport model. Perturbations are added to the true pseudo-observations of XCO_2 and the true fluxes, respectively, based on the corresponding error models. On that basis, we used the proposed core optimizer and a standard Bayesian inversion technique to obtain optimum estimates of the XCO_2 background concentration and the surface fluxes, respectively. Finally, we can evaluate the performance of the proposed method via comparison of estimates and truths of the background XCO_2 and the fluxes.

To explore the performance of the proposed method in the presence of different observation errors and *a priori* flux errors, 100 groups of experiments were designed, in which
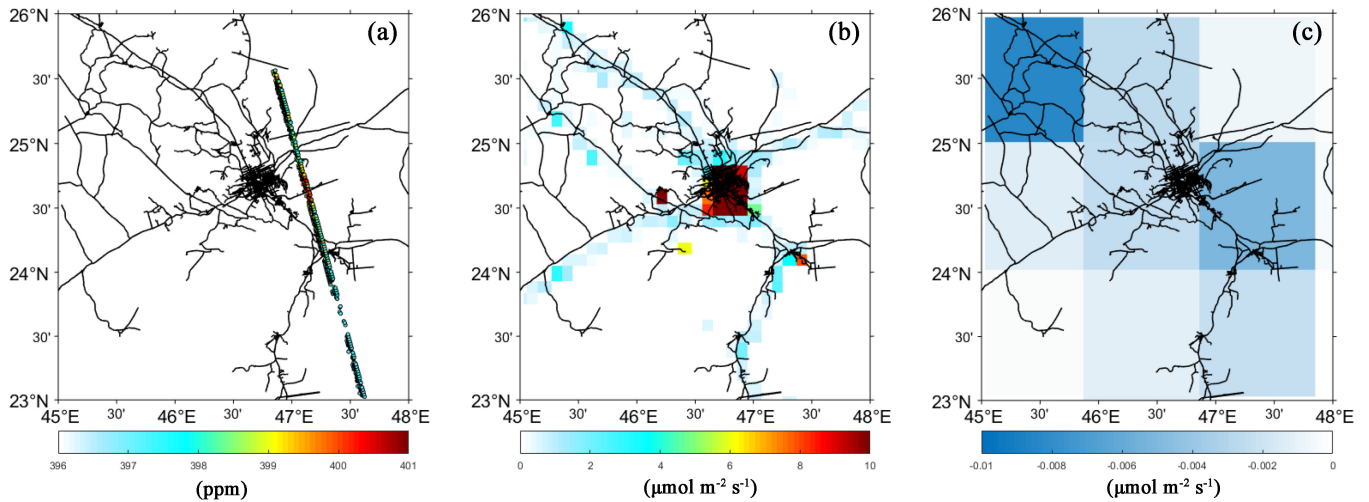
Fig. 2. (a) OCO-2' overpass near Riyadh on December 29, 2014. (b) and (c) FF fluxes from EDGAR and biogenic fluxes from Carbon Tracker for December 2014, respectively.

TABLE I
PARTIAL INFORMATION OF THE DATASETS USED IN THIS STUDY

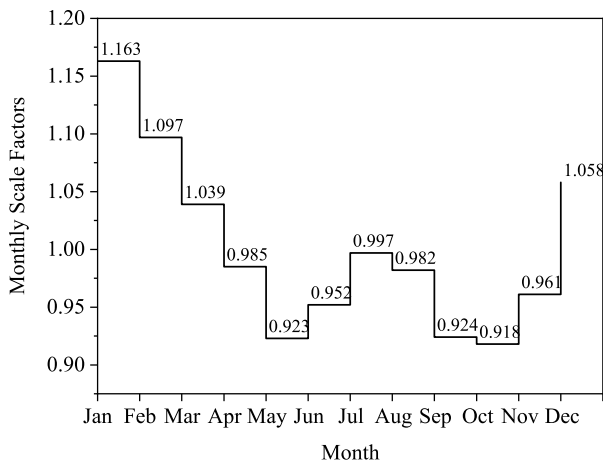| Product	Spatial resolution	Temporal resolution	Available date	Unit
XCO₂	1.29km×2.25km	16 days	2014-now	ppm
EDGAR	0.1°×0.1°	yearly	1970-2018	tonne km^{-2} month^{-1}
CT-NEE	1°×1°	3 hours	2000-2019	mol m^{-2} s^{-1}

Fig. 3. Monthly scaling factors derived from "Carbon Tracker."

η_1 indicates the improvement in terms of the true surface flux. η_2 indicates the improvement in terms of the error covariance of the *a priori* and *a posteriori*. μ_{delta} and σ_{delta} are used to directly describe the performance of the retrieved XCO₂ background. η_1 and η_2 are used to describe whether and to what extent the surface flux was improved. Theoretically, if the XCO₂ background was determined more accurately, inversions of the surface flux should also be more accurate.

E. Determination of Atmospheric Transport Model Errors

In OSSEs, we represent the errors in wind speed and direction by stretching or rotating the simulated XCO₂ plume along the average wind direction, following Ye *et al.* [16].

There are three common ways to represent atmospheric transport model errors when using real observation data: 1) comparison of the results of different atmospheric transport models [54]; 2) residuals between simulations and observations [55], [56]; and 3) quantifying the atmospheric transport model errors by directly comparing the simulated winds with the radiosonde data and incorporating the errors as random velocities in the air-packet trajectories [17], [36], [56]. In this study, we used a fractional uncertainty of 33% for the five overpasses due to horizontal and vertical transport assessed by Wu *et al.* [17]. The horizontal uncertainty was estimated by quantifying the effect of wind errors from radiosonde observations. The vertical uncertainty is determined by the variation in the enhancement values found for different rescaled PBL heights. A fractional uncertainty of 74% for a single overpass was obtained by multiplying the square root of 5 (the number of overpasses in Wu *et al.*'s [17] study). The same approach

observation errors vary from 0.1 to 1 ppm with a step of 0.1 ppm and *a priori* flux uncertainties vary from 10% to 100% with a step of 10%. For the observation errors, we have adopted a normal distribution model. The errors are assumed to be a random distribution with a mean of zero and a standard deviation of some specified value. Subsequently, for each group of experiments, 500 simulations were carried out.

To quantitatively evaluate the performance of the proposed method, we have designed four indicators, namely, μ_{delta}, σ_{delta}, η_1, and η_2. μ_{delta} and σ_{delta} denote the mean and the standard deviation of the differences between the retrieved and the truth XCO₂ background in each group of experiments.
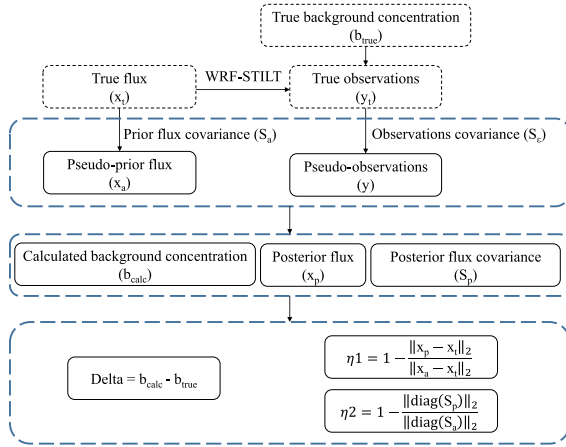
Fig. 4. Flowchart representing the overview of the OSSEs.

was used to represent atmospheric transport errors in the Middle East study by Yang *et al.* [36].

III. RESULTS

A. Observing System Simulation Experiments

Fig. 5 demonstrates the outcomes of simulation experiments based on the OSSEs. Fig. 5(a) shows that the retrieved background XCO_2 is the unbiased estimates of the true background XCO_2 regardless of observation errors of XCO_2 and *a priori* flux uncertainties. The maximum value of μ_{delta} is 0.01 ppm and occurs for a XCO_2 with an observation error of 1 ppm and *a priori* flux uncertainty of 60%. Overall, there is an increase in the absolute value of μ_{delta} as the XCO_2 observation error rises, although its magnitude is very small. In contrast, the uncertainty in surface fluxes has a much smaller effect on μ_{delta} and does not show a trending pattern.

Fig. 5(b) shows the sensitivity of σ_{delta} to the XCO_2 observations' error and the uncertainty of surface fluxes. Similar to Fig. 5(a), σ_{delta} is sensitive with the XCO_2 observation error and rises with an increase in the XCO_2 observation error. Meanwhile, σ_{delta} is insensitive with the uncertainty in surface fluxes. In general, σ_{delta} is kept below 0.05 ppm when the XCO_2 observation error is no more than 1 ppm. Consequently, we can conclude from the simulation experiments that the retrieved XCO_2 background using our proposed method is not only accurate but also precise.

Fig. 5(b) and (c) shows the sensitivity of η_1 and η_2 to the XCO_2 observation error and uncertainties of *a priori* surface fluxes. As shown in Fig. 4, both η_1 and η_2 take values in the range from 0 to 1. The closer they are to 1, the higher the degree of surface fluxes' optimization and vice versa. Both the figures show a similar pattern. The performances of optimized surface fluxes decrease with increasing XCO_2 observation error and increase with the decreasing *a priori* flux uncertainty. The latter outcomes may seem to be weird. This is because both the indicators, despite their differences, include in their definitions the uncertainty of *a priori* surface errors. From the point of view of definition, both the indicators are proportions rather than some absolute value. When the *a priori* error of surface fluxes is large, the greater the role played by the

XCO_2 observations in the inversion process and the easier it is to optimize the *a priori* error. It is worth noting that the uncertainty reduction is highly related to the intensity of footprint. As shown in Fig. 1, footprints exhibit an evidently spatial heterogeneity, which is mainly driven by wind fields. Hence, the uncertainty reduction actually also has an evidently spatial heterogeneity. In Fig. 5(c) and (d), η_1 and η_2 are the average of all uncertainty reductions in the whole study area. The grids with small footprint values pull down η_1 and η_2.

B. Experiments Based on Real Observations

As in the previous experiments with OSSEs, our study area is still the small spatial domain (from 45°E to 48°E, from 23°N to 26°N) adjacent to Riyadh. We selected five overpasses between 2014 and 2016.

1) Comparison of the Three Methods: First, we need to test how the proposed method performs against other existing methods. Silva and Arellano [23] chose a $4° \times 4°$ spatial region centered in a city and subtracted the standard deviation from the mean as the background concentration. Wu *et al.* [17] used the trajectory-endpoint method to estimate the XCO_2 background. As introduced in Section I, the existing background XCO_2 extraction methods can be categorized as the statistical method and the trajectory-endpoint method. The above-mentioned two methods are the representatives of these two categories, respectively. For comparison, we labeled the method used by Wu *et al.* [17] as $M1$ and the method used by Silva and Arellano [23] as $M2$. The proposed method in this work is abbreviated as $M3$.

We have selected XCO_2 products of OCO-2 on five different dates for our experiments. The outcomes of three different methods are demonstrated in Fig. 6. Overall, the XCO_2 backgrounds from the three different methods exhibit similar trends, but differ in values. $M2$ yielded the lowest XCO_2 background in all five cases. The difference between the maximum and minimum XCO_2 backgrounds obtained by three methods in five cases varies from 0.7 to 3 ppm, which is not a trivial value. The determination of the XCO_2 background directly affects the magnitude of XCO_2 enhancement which is the critical constraint for subsequent inversions of surface fluxes. Therefore, we can use three different XCO_2 background to implement the subsequent surface flux inversion, and then use the three *a posteriori* fluxes to simulate the XCO_2 observations, and finally compare these simulated XCO_2 with the observed XCO_2 from OCO-2 to evaluate the XCO_2 background extracted by different methods.

The *a posteriori* fluxes and simulated XCO_2 can be obtained using the three methods described above, the distribution of the difference between simulated XCO_2 using optimized surface fluxes, and the observed XCO_2 is shown in Fig. 7.

Except for the case on December 16, 2015, the $M3$ method provides a better match between the simulated and observed concentrations, not only with a normal distribution of μ equal to 0 but also with a smaller σ.

2) Spatial Distribution of Simulated and Observed XCO_2: Using the case of December 16, 2015 as an example, Fig. 8 shows the spatial distribution of the simulated and
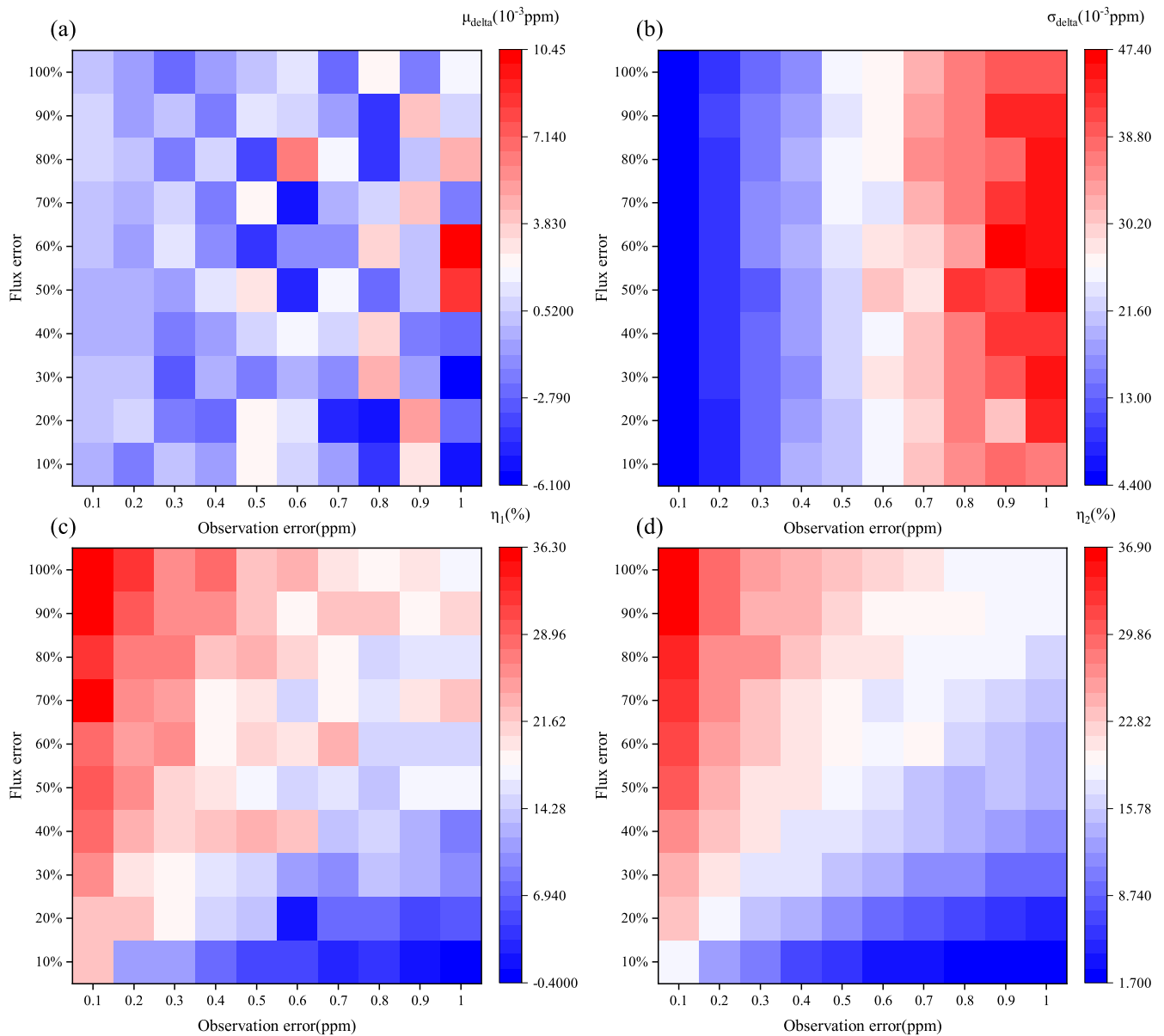
Fig. 5. Four indicators for evaluating the performance of the method. The horizontal axis represents the observation error of the satellite and the vertical axis represents the range of perturbation added to the true surface flux. Delta represents the difference between the calculated background concentration and the truth. (a) and (b) Mean value of delta and standard deviation of delta, respectively. (c) Degree of improvement of the posterior flux compared with the truth. (d) Degree of improvement of the posterior flux error covariance compared with the *a priori* flux error covariance.

observed XCO_2. Due to the lack of valid observations, we only selected areas with latitudes greater than 23.5°N to present the results. There are two simulated XCO_2. One is the simulated XCO_2 based on *a priori* surface fluxes and the other is that based on *a posteriori* surface fluxes. The *a posteriori* surface fluxes were optimized using XCO_2 background extracted by $M3$. Fig. 8 shows that there are significant XCO_2 enhancements near 24.25°N according to XCO_2 observations of OCO-2. The simulated XCO_2 based on *a priori* surface fluxes does not reproduce well in terms of the intensity of the XCO_2 enhancement. In contrast, the simulated XCO_2 using *a posteriori* CO_2 fluxes shows a better agreement with the observed XCO_2, especially in the range from about 23.6°N to 24.5°N. The typical difference between the simulated and observed XCO_2 decreased from over 2 to 1.13 ppm after

the optimization of surface CO_2 fluxes, implying a good performance of the extracted XCO_2 background.

3) Posterior CO_2 Flux and DOF: AK is the derivative function of the *a posteriori* flux about the *a priori* flux. Higher AK values are usually found where footprint values are high or where the *a priori* flux uncertainty is high, which means that less information is acquired from the *a priori* CO_2 fluxes [17]. The DOFs are the trace of AK matrix [34], which can be used to describe the amount of independent information provided by observations. Table II shows the differences between the *a priori* and *a posteriori* surface fluxes and the corresponding DOFs in each experiment. Table II shows that after optimization, the *a posteriori* surface fluxes vary in magnitude, ranging from −22% to 49%. The magnitude of the change is influenced not only by the confidence of observation (including uncertainty
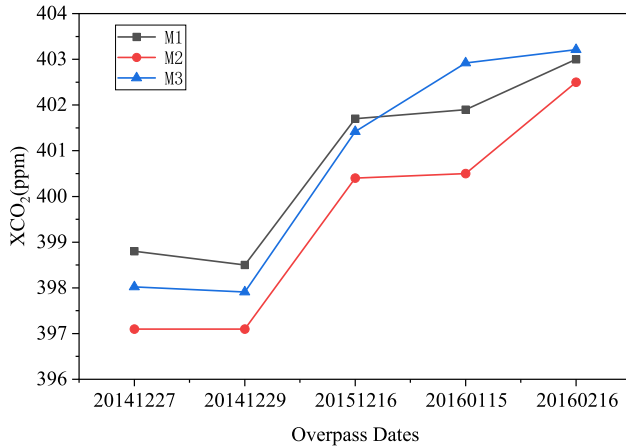
Fig. 6. Background XCO_2 calculated by three methods from 2014 to 2016 (the abscissa represents the date for the satellite to pass through Riyadh, and the gray rectangle, red circle, and blue triangle represent the background XCO_2 calculated by $M1$–$M3$, respectively).

TABLE III
EFFECT OF WIND ERROR ON METHOD ACCURACY

error sources		μ	σ
wind speed error (m/s)	1	-0.07	0.03
	2	-0.12	0.07
	4	-0.18	0.09
wind direction error (degree)	5	0.05	0.02
	10	0.09	0.05
	15	0.15	0.08

in atmospheric transport models and uncertainty in OCO-2 soundings) but also by the distribution of the footprint.

IV. DISCUSSION

A. Atmospheric Transport Model Errors

In the OSSEs, we analyzed the effect of different flux errors and observation errors on the method proposed in this study. However, these experiments are based on the assumption that the atmospheric transport model yields no errors. However, the error derived from the atmospheric transport model is not ignorable in many cases. Therefore, we focus on how uncertainties of outputs from the atmospheric transport model affect the extraction of XCO_2 background and the inversion of CO_2 fluxes in the section. In the specific experiment, the uncertainty of the CO_2 flux was set to 40% and the uncertainty of the XCO_2 observations was considered to be 1 ppm. We analyzed the effect of different wind speed and wind direction errors on the performances of the proposed method. The results are shown in Table III. Here, μ and σ are the mean and standard deviation of the difference between the calculated XCO_2 background and the true XCO_2 background, respectively. More observations of wind can help reduce the uncertainty of atmospheric transport. For example, the data assimilation system has been shown to be used to reduce errors in atmospheric transport in data-rich areas (e.g., Los Angeles) [57]. In addition to the systematic wind error, there will be positive/negative wind bias in some areas [16]. The X-STILT model proposed by Wu *et al.* [17] has the ability to correct for wind bias by rotating the model trajectory.

B. Limitation of OCO-2 Observations

Observations with high spatial coverage help obtain more accurate posterior fluxes for urban-scale study areas. For example, Ye *et al.* [16] showed that multi-track observations can effectively reduce the impact of non-systematic atmospheric transport errors on the inversion results. In this

study, an attempt was made to optimize *a priori* flux using OCO-2 observations, where the larger footprints ($>10^{-2}$) are usually distributed upwind of the satellite nadir point. However, for the city where there is a large deviation in the CO_2 flux it may not be corrected due to the distance from the satellite transit location or downwind. On the city scale, if the problem of a low spatial coverage can be solved, the ability to constrain fluxes by the top-down methods using spaceborne XCO_2 observations will be greatly improved.

Satellites operating in Sun-synchronous and low-earth polar orbits like OCO-2 provide a near-global coverage. However, they have a long revisit time, large gaps between adjacent tracks, and always look at the landscape at the same local time. Hence, they would eventually miss the daily changes in ecosystems. We have to rely on the time of day scaling factors to obtain the daily variation in CO_2 fluxes. The snapshot area map model of OCO-3 could be a useful tool for studying the urban carbon cycle [58]. Cities can be observed more frequently, providing an effective means of estimating urban carbon emissions. Whereas non-noon transit satellites are often constrained by the large solar zenith angle to obtain observations of solar radiance with a high SNR. Moreover, interferences from clouds and aerosols make the majority of passive remote sensing of XCO_2 invalid. In the forthcoming years, more satellites will be launched to measure GHGs from the space, such as China's Atmospheric Environment Monitoring Satellite (AEMS) [59] and GHG Satellites (GHGSS) [60], [61]. Those active remote sensing satellites can solve the above-mentioned shortcomings of passive remote sensing satellites.

The negative enhancement shown in Fig. 8 is also seen in similar previous studies [17], [36]. That may be due to biogenic fluxes, or it may be a measurement error of OCO-2. Although some biases due to systematic error have been removed in the bias-corrected data product. Wunch *et al.* [62] pointed out that residual biases that may be associated with surface properties and aerosol scattering still exist on a local scale, by comparison with the Total Carbon Column Observing Network (TCCON) XCO_2 measurements. Ye *et al.* noted that the effect of these biases on XCO_2 enhancement would be eliminated with the subtraction of the biased background XCO_2 in a small spatial domain (200–300 km) [16]. It is often the case that the tails surrounding the urban plume do not exactly match. Some studies selected representative (XCO_2 peaks) aggregated latitudinal band observations to reduce the effects of OCO-2 measurement errors and horizontal wind errors [16], [17]. Past versions (V8 and earlier)
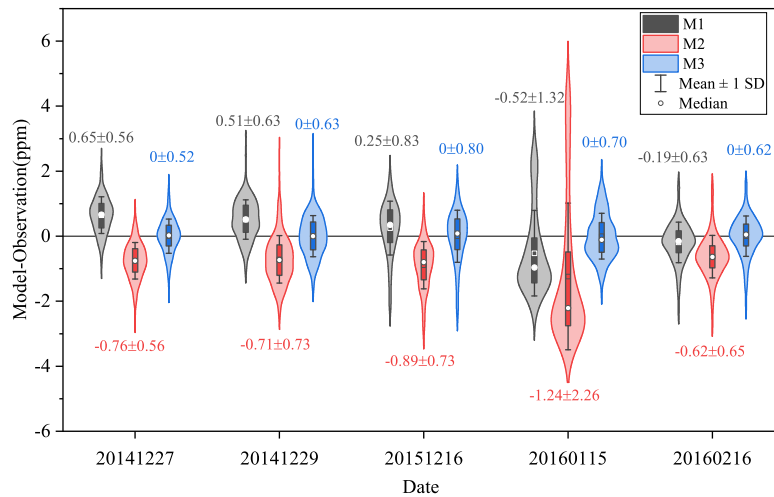
Fig. 7. Distribution of the difference between the simulated and observed XCO₂ in ppm. (Gray, red, and blue histograms represent the results obtained by the *M*1–*M*3 methods, respectively. The means and standard deviations of difference are shown in the legend).

TABLE II
RESULTS OF REAL CASES FOR FIVE TRACKS OVER RIYADH. BACKGROUND XCO₂ IS CALCULATED BY *M*3. PRIOR AND POSTERIOR REPRESENT THE AVERAGED PRIOR FLUXES AND POSTERIOR FLUX IN THE STUDY AREA (23°N–26°N, 45°E–48°E), RESPECTIVELY. CHANGE REPRESENTS THE CHANGE IN *a Posteriori* WHOLE-CITY EMISSIONS COMPARED WITH *a Priori* WHOLE-CITY EMISSIONS. DOF REPRESENTS THE DOF

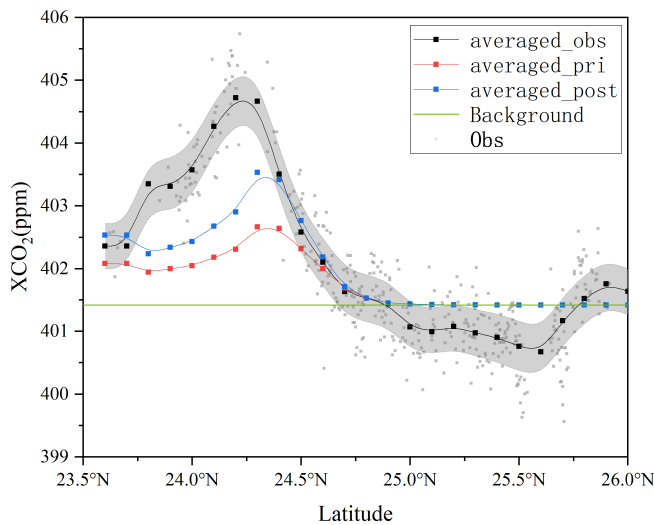| Time	Background XCO₂ (ppm)	A prior (Mt C d⁻¹)	A posterior (Mt C d⁻¹)	Change (%)	DOF
2014-12-27	398.02	72436	71302	-1.5652	0.8344
2014-12-29	397.91	72436	64641	-10.761	0.6890
2015-12-16	401.42	75252	112320	+49.2641	0.7759
2016-01-15	402.92	85058	66019	-22.3838	1.0131
2016-02-16	403.22	80218	71575	-10.7743	0.6977

Fig. 8. Demonstration of the relationship between XCO₂ and latitude. The gray squares represent OCO-2' observations, the green solid line represents the calculated background concentration, the black line represents the average of the observations per 0.1 degrees of latitude, the red line represents the simulated XCO₂ obtained by prior surface flux averaged per 0.1 degrees of latitude, and the blue line represents the average per 0.1 degrees obtained with the *a posteriori* flux.

of OCO-2 product could filter out the poorer quality data by warning levels, and after version 9 we can filter by "XCO₂_quality_flag." Poor quality observations are not recommended for use in flux inversions, which is risky. In addi-

tion, the OCO-2 team is constantly updating the versions of the data, and observations from different versions may have large differences [17], and we recommend using the latest version for CO₂ flux inversion. In this article, it is assumed that the results derived from OCO-2 observations are unbiased.

C. Configuration of Prior Error Covariance

The definition of *a priori* emission error is still subjective, and there is currently no strict quantification of emission error with a high resolution. A more accurate error covariance configuration facilitates a better flux estimation. However, it is very difficult to evaluate errors in *a priori* emission inventories [63], especially for pixel-level inversions, which usually requires comparing high-resolution accurate emission inventories (e.g., Vulcan [64] and Hestia [65] inventory). Furthermore, in pixel-level inversions, solving the spatial pattern requires additional information related to the spatial pattern of the *a priori* emission error. Basu *et al.* [66] proposed three ways to determine the correlation of spatial errors, which are exponential, regional, and a hybrid of the first two. Turner *et al.* [39] determined the *a priori* error covariance using the "hybrid" method and showed that a pixel-level inversion with multiple observation sites reasonably located in cities can effectively reduce the uncertainty of urban emissions and improve the spatial resolution of *a priori* emission inventories. Lauvaux *et al.* [67] also used the "hybrid" method and tested the impact on the *a posteriori* emissions using varying

correlation length. In contrast to the pixel-level inversion used in this article, some studies sacrifice the ability to capture spatial variability to obtain a whole-city scaling factor [16], [36]. This approach does not require consideration of spatial correlation.

D. Complexity of the Ecosystem

Riyadh with low vegetation was selected as the study area to reduce the influence of the uncertainty of biogenic fluxes on the experiment. More cities will be included in the future study. However, for cities with complex carbon sinks, it seems crucial to calculate accurate biogenic fluxes through excellent plant models (like Vegetation Photosynthesis and Respiration Model (VPRM) [68], [69] or Solar-Induced Fluorescence for Modeling Urban biogenic Fluxes (SMUrF) [70]) is necessary.

V. Summary and Conclusion

The estimation of regional XCO_2 background is the key to the CO_2 flux inversion with a good performance. In this article, a new method is proposed to calculate the XCO_2 background required by a standard and frequently used Bayesian inversion framework, considering the observation error of XCO_2 products and the error of the *a priori* flux. Moreover, the required calculation time is affordable. Hundred sets of sensitivity experiments (500 times for each group) show that: the bias and uncertainty of the XCO_2 background are below 0.01 and 0.05 ppm, respectively. When the observation error is 0.1 ppm and the flux uncertainty is 100%, the improvement of the *a posteriori* flux is up to 36.3% compared with the true flux, and the uncertainty reduction of the *a posteriori* flux is up to 36.9% compared with the *a priori* flux.

When there are errors in the atmospheric transport model, the flux optimization will become conservative due to the larger covariance of observation errors. To reduce the uncertainty derived from the atmospheric transport model, additional observations of the wind need to be considered.

Based on this method, we selected five overpasses from 2014 to 2016 to demonstrate a city-scale flux inversion near Riyadh. The comparison with the two previous methods shows that the posterior simulated XCO_2 by the method proposed in this work can match better with the observed XCO_2 from OCO-2. In addition, we found that EDGAR inventory overall overestimates Riyadh's emissions except December 16, 2015.

References

[1] R. K. Pachauri et al., *Climate Change 2014: Synthesis Report. Contribution of Working Groups I, II and III to the Fifth Assessment Report of the Intergovernmental Panel on Climate Change*. Geneva, Switzerland: IPCC, 2014.

[2] W. Peters et al., "An atmospheric perspective on North American carbon dioxide exchange: CarbonTracker," *Proc. Nat. Acad. Sci. USA*, vol. 104, no. 48, pp. 18925–18930, 2007.

[3] K. R. Gurney et al., "Reconciling the differences between a bottom-up and inverse-estimated FFCO2 emissions estimate in a large U.S. Urban area," *Elementa: Sci. Anthropocene*, vol. 5, p. 44, Jan. 2017.

[4] J. Brioude et al., "Top-down estimate of surface flux in the Los Angeles Basin using a mesoscale inverse modeling technique: Assessing anthropogenic emissions of CO, NO_x and CO_2 and their impacts," *Atmos. Chem. Phys.*, vol. 13, no. 7, pp. 3661–3677, 2013.

[5] C. Hu et al., "Top-down constraints on anthropogenic CO_2 emissions within an agricultural-urban landscape," *J. Geophys. Res., Atmos.*, vol. 123, no. 9, pp. 4674–4694, 2018.

[6] H. Eggleston, L. Buendia, K. Miwa, T. Ngara, and K. Tanabe, "2006 IPCC guidelines for national greenhouse gas inventories," Change IPO, Inst. Global Environ. Strategies, Hayama, OL, Japan, Tech. Rep., 2006.

[7] J. G. J. Olivier and J. A. H. W. Peters, "Trends in global CO_2 and total greenhouse gas emissions," PBL Netherlands Environ. Assessment Agency, The Hague, Tech. Rep. 2674, 2017.

[8] L. Zhu et al., "Reduced carbon emission estimates from fossil fuel combustion and cement production in China," *Nature*, vol. 524, no. 7565, pp. 335–338, Aug. 2015.

[9] P. Peylin et al., "Global atmospheric carbon budget: Results from an ensemble of atmospheric CO_2 inversions," *Biogeosciences*, vol. 10, no. 10, pp. 6699–6720, 2013.

[10] R. Wang et al., "High-resolution mapping of combustion processes and implications for CO_2 emissions," *Atmos. Chem. Phys.*, vol. 13, no. 10, pp. 5189–5203, 2013.

[11] E. A. Kort, W. M. Angevine, R. Duren, and C. E. Miller, "Surface observations for monitoring urban fossil fuel CO_2 emissions: Minimum site location requirements for the Los Angeles megacity," *J. Geophys. Res., Atmos.*, vol. 118, no. 3, pp. 1577–1584, 2013.

[12] K. McKain, S. C. Wofsy, T. Nehrkorn, J. Eluszkiewicz, J. R. Ehleringer, and B. B. Stephens, "Assessment of ground-based atmospheric observations for verification of greenhouse gas emissions from an urban region," *Proc. Nat. Acad. Sci. USA*, vol. 109, no. 22, pp. 8423–8428, 2012.

[13] A. Luther et al., "Quantifying CH_4 emissions from hard coal mines using mobile sun-viewing Fourier transform spectrometry," *Atmos. Meas. Techn.*, vol. 12, no. 10, pp. 5217–5230, 2019.

[14] G. Ehret, C. Kiemle, M. Wirth, A. Amediek, A. Fix, and S. Houweling, "Space-borne remote sensing of CO_2, CH_4, and N_2O by integrated path differential absorption lidar: A sensitivity analysis," *Appl. Phys. B*, vol. 90, no. 3, pp. 593–608, 2008.

[15] M. Buchwitz et al., "Global satellite observations of column-averaged carbon dioxide and methane: The GHG-CCI XCO_2 and XCH_4 CRDP3 data set," *Remote Sens. Environ.*, vol. 203, pp. 276–295, Dec. 2017.

[16] X. Ye et al., "Constraining fossil fuel CO_2 emissions from urban area using OCO-2 observations of total column CO_2," *J. Geophys. Res., Atmos.*, vol. 125, no. 8, 2020, Art. no. e2019JD030528.

[17] D. Wu et al., "A Lagrangian approach towards extracting signals of urban CO_2 emissions from satellite observations of atmospheric column CO_2 (XCO_2): X-stochastic time-inverted Lagrangian transport model ('X-STILT v1')," *Geosci. Model Develop.*, vol. 11, no. 12, pp. 4843–4871, 2018.

[18] B. Zheng et al., "Observing carbon dioxide emissions over China's cities and industrial areas with the orbiting carbon observatory-2," *Atmos. Chem. Phys.*, vol. 20, no. 14, pp. 8501–8510, Jul. 2020.

[19] F. M. Schwandner et al., "Spaceborne detection of localized carbon dioxide sources," *Science*, vol. 358, no. 6360, Oct. 2017, Art. no. eaam5782.

[20] R. Nassar, T. G. Hill, C. A. McLinden, D. Wunch, D. B. Jones, and D. Crisp, "Quantifying CO_2 emissions from individual power plants from space," *Geophys. Res. Lett.*, vol. 44, no. 19, pp. 10045–10053, 2017.

[21] A. Karion *et al.*, "Investigating Alaskan methane and carbon dioxide fluxes using measurements from the CARVE tower," *Atmos. Chem. Phys.*, vol. 16, no. 8, pp. 5383–5398, Apr. 2016.

[22] J. Hakkarainen, I. Ialongo, and J. Tamminen, "Direct space-based observations of anthropogenic CO_2 emission areas from OCO-2," *Geophys. Res. Lett.*, vol. 43, no. 21, pp. 11400–11406, 2016.

[23] S. J. Silva and A. Arellano, "Characterizing regional-scale combustion using satellite retrievals of CO, NO_2 and CO_2," *Remote Sens.*, vol. 9, no. 7, p. 744, 2017.

[24] E. A. Kort, C. Frankenberg, C. E. Miller, and T. Oda, "Space-based observations of megacity carbon dioxide," *Geophys. Res. Lett.*, vol. 39, no. 17, Sep. 2012.

[25] O. Schneising, J. Heymann, M. Buchwitz, M. Reuter, H. Bovensmann, and J. P. Burrows, "Anthropogenic carbon dioxide source areas observed from space: Assessment of regional enhancements and trends," *Atmos. Chem. Phys.*, vol. 13, no. 5, pp. 2445–2454, Mar. 2013.

[26] J. C. Lin, D. V. Mallia, D. Wu, and B. B. Stephens, "How can mountaintop CO_2 observations be used to constrain regional carbon fluxes?" *Atmos. Chem. Phys.*, vol. 17, no. 9, pp. 5561–5581, 2017.

[27] R. Macatangay *et al.*, "A framework for comparing remotely sensed and *in-situ* CO_2 concentrations," *Atmos. Chem. Phys.*, vol. 8, no. 9, pp. 2555–2568, 2008.

[28] D. Mallia, J. Lin, S. Urbanski, J. Ehleringer, and T. Nehrkorn, "Impacts of upwind wildfire emissions on CO, CO_2, and $PM_{2.5}$ concentrations in Salt Lake City, Utah," *J. Geophys. Res., Atmos.*, vol. 120, no. 1, pp. 147–166, 2015.

[29] M. L. Fischer *et al.*, "Simulating estimation of California fossil fuel and biosphere carbon dioxide exchanges combining *in situ* tower and satellite column observations," *J. Geophys. Res., Atmos.*, vol. 122, no. 6, pp. 3653–3671, Mar. 2017.

[30] J. C. Lin, "A near-field tool for simulating the upstream influence of atmospheric observations: The stochastic time-inverted Lagrangian transport (STILT) model," *J. Geophys. Res.*, vol. 108, no. D16, 2003.

[31] B. Liu *et al.*, "The relationship between atmospheric boundary layer and temperature inversion layer and their aerosol capture capabilities," *Atmos. Res.*, vol. 271, p. 106121, 2022.

[32] V. Yesubabu, C. V. Srinivas, S. Langodan, and I. Hoteit, "Predicting extreme rainfall events over Jeddah, Saudi Arabia: Impact of data assimilation with conventional and satellite observations," *Quart. J. Roy. Meteorol. Soc.*, vol. 142, no. 694, pp. 327–348, Jan. 2016.

[33] W. C. Skamarock *et al.*, "A description of the advanced research WRF model version 4.3," Tech. Rep. NCAR/TN-556+STR, 2021, doi: 10.5065/1dfh-6p97.

[34] B. J. Connor, H. Boesch, G. Toon, B. Sen, C. Miller, and D. Crisp, "Orbiting carbon observatory: Inverse method and prospective error analysis," *J. Geophys. Res., Atmos.*, vol. 113, no. D5, Mar. 2008.

[35] D. Crisp *et al.*, "The orbiting carbon observatory (OCO) mission," *Adv. Space Res.*, vol. 34, no. 4, pp. 700–709, 2004.

[36] E. G. Yang *et al.*, "Using space-based observations and Lagrangian modeling to evaluate urban carbon dioxide emissions in the Middle East," *J. Geophys. Res., Atmos.*, vol. 125, no. 7, 2020, Art. no. e2019JD031922.

[37] Y. Villalobos, P. Rayner, S. Thomas, and J. Silver, "The potential of orbiting carbon observatory-2 data to reduce the uncertainties in CO_2 surface fluxes over Australia using a variational assimilation scheme," *Atmos. Chem. Phys.*, vol. 20, no. 14, pp. 8473–8500, 2020.

[38] C. D. Rodgers, *Inverse Methods for Atmospheric Sounding: Theory and Practice*, vol. 2. Singapore: World Scientific, 2000.

[39] A. J. Turner, A. A. Shusterman, B. C. McDonald, V. Teige, R. A. Harley, and R. C. Cohen, "Network design for quantifying urban CO_2 emissions: Assessing trade-offs between precision and network density," *Atmos. Chem. Phys.*, vol. 16, no. 21, pp. 13465–13475, 2016.

[40] A. J. Turner, D. J. Jacob, J. Benmergui, J. Brandman, L. White, and C. A. Randles, "Assessing the capability of different satellite observing configurations to resolve the distribution of methane emissions at kilometer scales," *Atmos. Chem. Phys.*, vol. 18, no. 11, pp. 8265–8278, Jun. 2018.

[41] T. Lauvaux *et al.*, "Constraining the CO_2 budget of the corn belt: Exploring uncertainties from the assumptions in a mesoscale inverse system," *Atmos. Chem. Phys.*, vol. 12, no. 1, pp. 337–354, 2012.

[42] J. F. Meirink, P. Bergamaschi, and M. C. Krol, "Four-dimensional variational data assimilation for inverse modelling of atmospheric methane emissions: Method and comparison with synthesis inversion," *Atmos. Chem. Phys.*, vol. 8, no. 21, pp. 6341–6353, Nov. 2008.

[43] L. Wu *et al.*, "What would dense atmospheric observation networks bring to the quantification of city CO_2 emissions?" *Atmos. Chem. Phys.*, vol. 16, no. 12, pp. 7743–7771, 2016.

[44] S. Al-Hathloul *et al.*, "Riyadh development plans in the past fifty years (1967–2016)," *Current Urban Stud.*, vol. 5, no. 1, p. 97, 2017.

[45] T. Boden, R. Andres, and G. Marland, "Global, regional, and national fossil-fuel CO_2 emissions (1751–2013)(v. 2016) [Data set]," Environ. Syst. Sci. Data Infrastruct. Virtual Ecosyst., Carbon Dioxide Inf. Analysis Center, Oak Ridge Nat. Lab., Oak Ridge, TN, USA, Tech. Rep., 2016, doi: 10.3334/cdiac/00001_v2016.

[46] B. Connor *et al.*, "Quantification of uncertainties in OCO-2 measurements of XCO_2: Simulations and linear error analysis," *Atmos. Meas. Techn.*, vol. 9, no. 10, pp. 5227–5238, 2016.

[47] A. Liang, W. Gong, G. Han, and C. Xiang, "Comparison of satellite-observed XCO_2 from GOSAT, OCO-2, and ground-based TCCON," *Remote Sens.*, vol. 9, no. 10, p. 1033, Oct. 2017.

[48] D. Crisp, "NASA orbiting carbon observatory: Measuring the column averaged carbon dioxide mole fraction from space," *J. Appl. Remote Sens.*, vol. 2, no. 1, Mar. 2008, Art. no. 023508.

[49] M. Gunson and A. Eldering, "OCO-2 level 2 bias-corrected XCO_2 and other select fields from the full-physics retrieval aggregated as daily files, retrospective processing V8r Greenbelt, MD, USA, Goddard Earth sciences data and information services center (GES DISC)," OCO-2 Science Team, Tech. Rep., 2018. [Online]. Available: https://disc.gsfc.nasa.gov/datasets/OCO2_L2_Lite_FP_10r/summary?keywords=OCO2

[50] M. Crippa *et al.* (2019). *Edgar V5. 0 Global Air Pollutant Emissions*. European Commission, Joint Research Center (JRC)[Dataset] PID. [Online]. Available: http://data.europa.eu/89h/377801af-b094-4943-8fdc-f79a7c0c2d19

[51] J. Yuan, Z. Niu, and C. Wang, "Vegetation NPP distribution based on MODIS data and CASA model—A case study of northern Hebei Province," *Chin. Geographical Sci.*, vol. 16, no. 4, pp. 334–341, 2006.

[52] T. N. Carlson and D. A. Ripley, "On the relation between NDVI, fractional vegetation cover, and leaf area index," *Remote Sens. Environ.*, vol. 62, no. 3, pp. 241–252, 1997.

[53] F. Chevallier *et al.*, "CO_2 surface fluxes at grid point scale estimated from a global 21 year reanalysis of atmospheric measurements," *J. Geophys. Res., Atmos.*, vol. 115, no. D21, 2010.

[54] K. R. Gurney *et al.*, "Towards robust regional estimates of CO_2 sources and sinks using atmospheric transport modelsmodels," *Nature*, vol. 415, no. 6872, pp. 626–630, 2002.

[55] N. M. Mahowald, R. G. Prinn, and P. J. Rasch, "Deducing CCl3F emissions using an inverse method and chemical transport models with assimilated winds," *J. Geophys. Res., Atmos.*, vol. 102, no. D23, pp. 28153–28168, Dec. 1997.

[56] W. Xu, W. Wang, N. Wang, and B. Chen, "A new algorithm for Himawari-8 aerosol optical depth retrieval by integrating regional PM2.5 concentrations," *IEEE Trans. Geosci. Remote Sens.*, to be published, doi: 10.1109/TGRS.2022.3155503.

[57] A. Deng *et al.*, "Toward reduced transport errors in a high resolution urban CO_2 inversion system," *Elementa: Sci. Anthropocene*, vol. 5, Jan. 2017.

[58] A. Eldering, T. E. Taylor, C. W. O'Dell, and R. Pavlick, "The OCO-3 mission: Measurement objectives and expected performance based on 1 year of simulated data," *Atmos. Meas. Techn.*, vol. 12, no. 4, pp. 2341–2370, Apr. 2019.

[59] G. Han *et al.*, "Feasibility study on measuring atmospheric CO_2 in urban areas using spaceborne CO_2-IPDA LIDAR," *Remote Sens.*, vol. 10, no. 7, p. 985, Jun. 2018.

[60] G. Han *et al.*, "Performance evaluation for China's planned CO_2-IPDA," *Remote Sens.*, vol. 9, no. 8, p. 768, 2017.

[61] T. Shi *et al.*, "Quantifying CO_2 uptakes over oceans using LIDAR: A tentative experiment in Bohai bay," *Geophys. Res. Lett.*, vol. 48, no. 9, 2021, Art. no. e2020GL091160.

[62] D. Wunch *et al.*, "Comparisons of the orbiting carbon observatory-2 (OCO-2) XCO_2 measurements with TCCON," *Atmos. Meas. Techn.*, vol. 10, no. 6, pp. 2209–2238, 2017.

[63] R. J. Andres, T. A. Boden, and D. M. Higdon, "Gridded uncertainty in fossil fuel carbon dioxide emission maps, a CDIAC example," *Atmos. Chem. Phys.*, vol. 16, no. 23, pp. 14979–14995, Dec. 2016.

[64] K. R. Gurney *et al.*, "High resolution fossil fuel combustion CO_2 emission fluxes for the United States," *Environ. Sci. Technol.*, vol. 43, no. 14, pp. 5535–5541, Jul. 2009.

[65] K. Gurney *et al.*, "Vulcan and Hestia: High resolution quantification of fossil fuel CO_2 emissions," in *Proc. 19th Int. Congr. Modelling Simulation-Sustaining Our Future: Understand. Living Uncertainty (MODSIM)*, 2011, pp. 1781–1787.

[66] S. Basu, J. B. Miller, and S. Lehman, "Separation of biospheric and fossil fuel fluxes of CO_2 by atmospheric inversion of CO_2 and $^{14}CO_2$ measurements: Observation system simulations," *Atmos. Chem. Phys.*, vol. 16, no. 9, pp. 5665–5683, 2016.

[67] T. Lauvaux *et al.*, "High-resolution atmospheric inversion of urban CO_2 emissions during the dormant season of the Indianapolis Flux Experiment (INFLUX)," *J. Geophys. Res., Atmos.*, vol. 121, no. 10, pp. 5213–5236, 2016.

[68] P. Mahadevan *et al.*, "A satellite-based biosphere parameterization for net ecosystem CO_2 exchange: Vegetation photosynthesis and respiration model (VPRM)," *Global Biogeochem. Cycles*, vol. 22, no. 2, 2008.

[69] B. Luo *et al.*, "Target classification of similar spatial characteristics in complex urban areas by using multispectral LiDAR," *Remote Sens.*, vol. 14, p. 238, 2022, doi: 10.3390/rs14010238.

[70] D. Wu *et al.*, "A model for urban biogenic CO_2 fluxes: Solar-induced fluorescence for modeling urban biogenic fluxes (SMUrF v1)," *Geosci. Model Develop.*, vol. 14, no. 6, pp. 3633–3661, 2021.

Zhipeng Pei received the B.S. degree from Wuhan University, Wuhan, China, in 2019, where he is currently pursuing the Ph.D. degree with the State Key Laboratory of Information Engineering in Surveying, Mapping and Remote Sensing.

His research interests include satellite remote sensing, numerical modeling, Bayesian inversion, and machine learning.

Ge Han received the B.S. and M.S. degrees in geodetection and information technology from the China University of Geosciences, Wuhan, China, in 2009 and 2012, respectively, and the Ph.D. degree in remote sensing from the State Key Laboratory of Information Engineering in Surveying, Mapping and Remote Sensing, Wuhan University, Wuhan, in 2015.

He is currently an Assistant Professor with the School of Remote Sensing and Information Engineering, Wuhan University. His research interests include atmospheric sounding and remote sensing of environment.

Xin Ma received the B.S., M.S., and Ph.D. degrees from Wuhan University, Wuhan, China, in 2010, 2013, and 2016, respectively.

He is currently an Assistant Professor with the State Key Laboratory of Information Engineering in Surveying, Mapping and Remote Sensing, Wuhan University. His research interests include light detection and ranging (LIDAR) and atmospheric remote sensing.

Tianqi Shi received the B.S. degree from Henan Polytechnic University, Jiaozuo, Henan, China, in 2017. He is currently pursuing the M.S. degree in remote sensing with the State Key Laboratory of Information Engineering in Surveying, Mapping and Remote Sensing, Wuhan University, Wuhan, China.

His research interests include atmospheric sounding and remote sensing of environment.

Wei Gong (Member, IEEE) received the B.S. degree in photonics engineering from the Huazhong University of Science and Technology (HUST), Wuhan, China, in 1993, the M.S. degree in electronics from the Chinese Academy of Sciences, Lanzhou, China, in 1996, and the Ph.D. degree in physical electronics from HUST in 1999.

He was an Assistant Professor with Hampton University, Hampton, VA, USA, from 2002 to 2004. He is currently a Professor with the State Key Laboratory of Information Engineering in Surveying, Mapping and Remote Sensing, Wuhan University, Wuhan. He is involved in teaching and research of new laser, optical technology, and its remote sensing applications, and has made achievements in atmospheric light detection and ranging (LIDAR) and optical remote sensing. He has authored more than 100 scientific articles, holds 18 patents, and has coauthored two books.

Dr. Gong was a recipient of the New Century Excellent Talents in 2007, the Luojia Scholars, the Chutian Scholars in 2010, and the Yangtze River Scholars in 2014.